

Propeller tip and hub vortex dynamics in the interaction with a rudder

Mario Felli · Massimo Falchi

Received: 8 March 2011 / Revised: 10 June 2011 / Accepted: 30 June 2011 / Published online: 10 July 2011
© Springer-Verlag 2011

Abstract In the present paper, the interaction mechanisms of the vortices shed by a single-screw propeller with a rudder installed in its wake are addressed; in particular, following the works by Felli et al. (Exp Fluids 6(1):1–11, 2006a, Exp Fluids 46(1):147–1641, 2009a, Proceedings of the 8th international symposium on particle image velocimetry: Piv09, Melbourne, 2009b), the attention is focused on the analysis of the evolution, instability, breakdown and recovering mechanisms of the propeller tip and hub vortices during the interaction with the rudder. To investigate these mechanisms in detail, a wide experimental activity consisting in time-resolved visualizations, velocity measurements by particle image velocimetry (PIV) and laser Doppler velocimetry (LDV) along horizontal chordwise, vertical chordwise and transversal sections of the wake have been performed in the Cavitation Tunnel of the Italian Navy. Collected data allows to investigate the major flow features that distinguish the flow field around a rudder operating in the wake of a propeller, as, for example, the spiral breakdown of the vortex filaments, the rejoining mechanism of the tip vortices behind the rudder and the mechanisms governing the different spanwise misalignment of the vortex filaments in the pressure and suction sides of the appendage.

1 Introduction

Over the past decades, non-intrusive optical diagnostic tools have provided much insight in the field of marine

propulsion, allowing the performance improvement of propelled units and supporting the research toward the understanding of complex phenomena, not yet documented in literature thoroughly.

A typical scenario concerns the reduction of the propeller-induced perturbation on the hull and, in particular, the problem of the propeller–rudder interaction that represents an issue of relevance for its strict correlation to the hydro-acoustic, structural and propulsive performance of the ship. In fact, the installation of the rudder in the wake of a propeller is the cause of a number of problems as, for instance, the occurrence of cavitation on the rudder surface even at the low speed operations, the periodic impact of the propeller vortical structures, the periodic nature of the side force due to the nonuniform distribution of the hydrodynamic load. In this scenario, the demand for the performance improvement has implied a rising interest into detailed numerical and experimental tools, used to support new design configurations, as in the case of the twisted rudder (Shen et al. 1997a, b), as well as to get a better insight into the complex mechanisms distinguishing the dynamics of the propeller vortical structures during the interaction with the rudder. However, such an accurate analysis is still a challenging task, especially when the influence of the propeller is important and requires advanced numerical and experimental tools to resolve such a complex flow field with the adequate accuracy. More specifically, such a complexity is correlated to the marked turbulent, unsteady, 3-D and, in given situations, multi-phase nature of the flow around the rudder, which is dominated by the large-scale coherent structures of the propeller wake.

On the experimental side, the problem of the propeller–rudder interaction has been quite addressed by literature, even if the attained evidence of the distinguishing

M. Felli (✉) · M. Falchi
CNR-INSEAN, Italian Ship Model Basin,
Via di Vallerano 139, 00128 Rome, Italy
e-mail: m.felli@insean.it

phenomena has been mostly qualitative, being the results of visualization campaigns or global measurements, as in Kracht (1992), Molland and Turnock (1992), Shen et al. (1997a, b), Paik et al. (2008).

Few have been the works dealing with the measure of the flow field distribution around a rudder instead, e.g., Felli and Di Felice (2004), Felli et al. (2009a, b), Anschau and Mach (2009), Lücke and Streckwall (2009). Most of these studies has regarded the application of circumferential-averaged (Shen et al. 1997a) and phase-locked (Felli and Di Felice 2004; Felli et al. 2009a) LDV measurements almost exclusively that allowed resolving the flow field around the rudder on average only and thus, revealed little effective for the thoroughly understanding of the mechanisms driving the dynamic of the propeller vortical structures. In this regard, the two-dimensional nature of the PIV techniques (e.g., 2-D-PIV, Stereo-PIV, TR PIV) allows overcoming the above limitations, with a drastic reduction of the testing time and cost, as well.

In particular, the study by Felli et al. (2009a) allowed highlighting major phenomena characterizing the complex dynamics of the propeller tip vortices during the interaction with the rudder such as, for example, the mechanism of penetration at the leading edge region of the rudder, the double-helix instability and the reconnection mechanism after passing the rudder trailing edge. However, a part from the analysis of the overall evolution of the wake in transversal planes just in front and behind the rudder, in which phase-locked LDV was used, most of this information was qualitative and concerned time-resolved visualizations of the cavitating tip vortices.

Following Felli et al. (2009a), the present paper puts more emphasis onto quantitative aspects investigating the interaction mechanisms between the propeller wake and the rudder by means of detailed phase-locked PIV and LDV measurements of the velocity field. Unlike the experiments by Felli et al. (2009a), in the present study the adopted propeller–rudder configuration was designed to simulate the typical arrangement of a single-screw ship model, and, thus, concerned the rudder fixed with the plane of symmetry passing through the prolongation of the propeller axis. Specifically, the experimental analysis of the flow field around the propeller–rudder configuration includes:

- PIV measurements along horizontal chordwise and vertical chordwise sections of the wake, covering the area from the propeller plane down to about one rudder chord behind the rudder.
- LDV measurements along transversal sections just in front of and behind the rudder and all along the rudder surface.
- Near-wall LDV measurements along the rudder surface.

The paper is organized according to the following outline. In Sect. 2, we deal with the description of the experimental configuration and the set ups of the LDV and PIV measurements. In Sect. 3, we describe the test matrix and conditions. The analysis of the results is documented in Sect. 4. Conclusions are summarized in Sect. 5.

2 Experimental set-up and techniques

2.1 Experimental facility

Measurements have been conducted in the Cavitation Tunnel of the Italian Navy. This is a close jet tunnel with a 2.6 m length by 0.6 m width by 0.6 m height test section. Perspex windows on the four walls enable the optical access in the test section. Window thickness is 30 mm. The nozzle contraction ratio is 5.96:1 and the maximum water speed is 12 m/s. The highest free-stream turbulence intensity in the test section is 2%. In the test section, the mean velocity uniformity is within 1% for the axial component and 3% for the vertical component.

2.2 Rudder and propeller geometries and set up

The main goal of the present investigation is to accurately describe the fundamental mechanisms driving the interaction between the coherent structures of the propeller wake and the rudder. In this regard, a simple propeller–rudder geometry was designed to avoid that complicated and unknown flow features could get the flow field difficult to be understood.

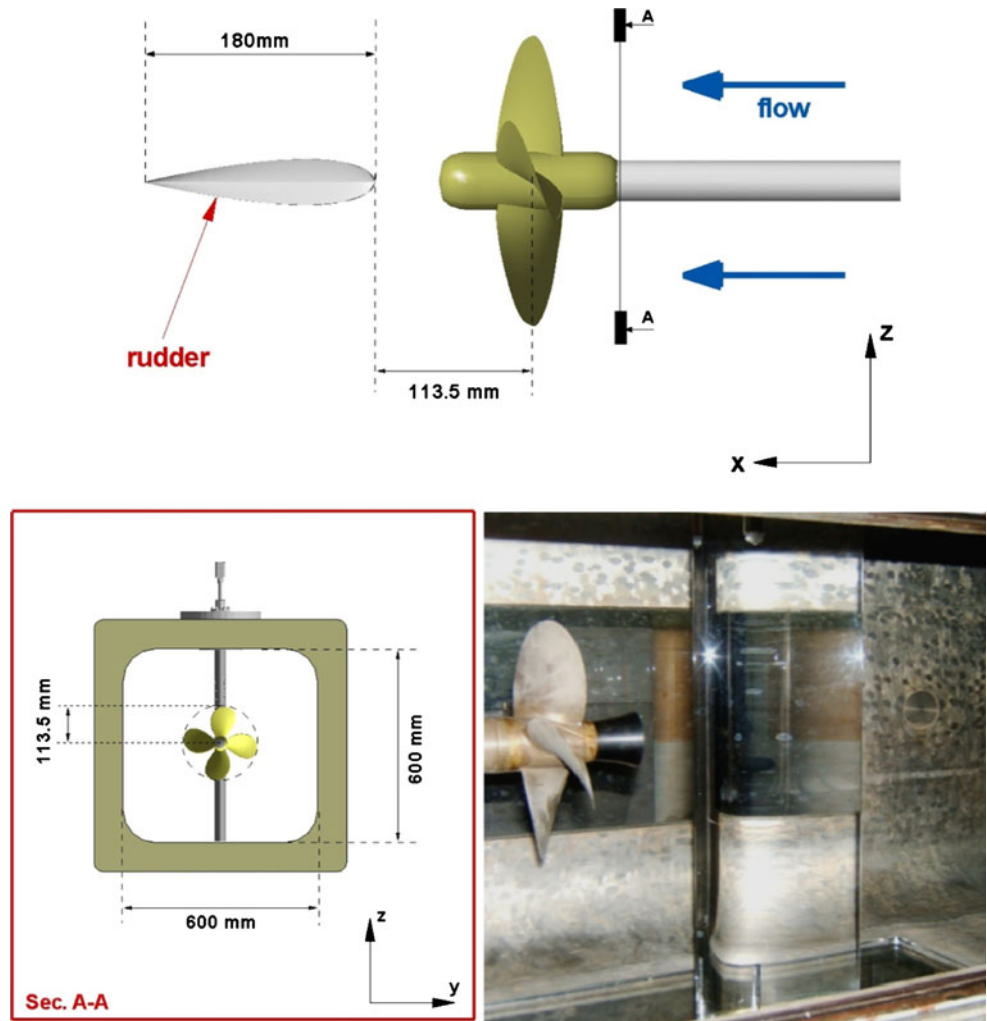
The rudder geometry was simulated using an all movable 2-D wing having a rectangular planform with 180-mm chord and 600-mm span and standard symmetric sections with NACA 0020 profile. The choice of a 2-D rudder was to limit the rising of the wing tip vortices and their interaction with the ones coming from the propeller. Moreover, simple geometries are fully adequate to provide CFD code validation datasets.

The rudder was manufactured in Perspex to allow the laser light sheet passing through it and, thus, simultaneous measurements on both sides to be performed.

The propeller–rudder arrangement was thought to simulate the typical configuration of a single-screw ship model. Therefore, the rudder was fixed with the plane of symmetry passing through the prolongation of the propeller axis and with the leading edge at about $r = R$ from the propeller disk plane. A sketch of the experimental configuration is given in Fig. 1.

The propeller used for current activity was the INSEAN E779a model; this is a model of a Wageningen-modified

Fig. 1 Propeller–rudder configuration. *Picture* shows the perspex model of the rudder



type, four-bladed, fixed-pitch, right-handed propeller characterized by a nominally constant pitch distribution and a very low skew. Details of the propeller geometry are described in Table 1. The choice of this propeller model was motivated by knowledge on the fluid-dynamic field based on a large experimental hydrodynamic and hydroacoustic available data set (Stella et al. 2000; Di Felice et al. 2004; Felli et al. 2006a, b, 2009a, b).

Table 1 Dimensions of the INSEAN E779A model propeller

Propeller diameter	$D = 227 \text{ mm}$
Number of blades	$Z = 4$
Pitch ratio	$P/D = 1.1$
Rake	$I = 4^{\circ}35'$ (forward)
Expanded area ratio	$EAR = 0.69$
Hub diameter (at prop. Ref. line)	$D_{\text{hub}} = 45.53 \text{ mm}$

2.3 Reference frames and dimensionless groups

Two reference systems were adopted:

- A Cartesian reference frame $O\text{-}XYZ$ with the origin O at the intersection between the propeller disk and the propeller axis, the X axis downstream-oriented along the tunnel centerline, the Y axis along the upward vertical, the Z axis along the horizontal toward starboard.
- A cylindrical reference frame $O\text{-}XR\theta$ with the origin O in the intersection between the propeller disk and the propeller axis, the X axis downstream-oriented along the propeller axis, the R axis along the radial outward, the azimuthal coordinate, θ , counter clockwise positive.

Two dimensionless groups govern the flow field around a propeller–rudder configuration in non-cavitating conditions: the advance ratio $J = U_{\infty}/2nR$, where U_{∞} is the free-stream velocity, n the revolution frequency and $2R$ the

propeller diameter and the Reynolds number $Re = cU_\infty/\nu$, where c is the rudder chord and ν the kinematic viscosity.

2.4 Velocity measurements

2.4.1 PIV experimental set-up

A sketch of the PIV experimental set-up is shown in Fig. 2. Rudder was mounted on the side window of the facility, parallel to the optical axis of two CCD cameras (i.e., PCO Sencam $1,028 \times 1,280$ px²) to investigate the horizontal chordwise sections of the wake, and on the top and bottom sides of the facility for the vertical sections. The two camera arrangement has been selected to increase the total region of interest without jeopardizing the spatial resolution of the measurement. Furthermore, the arrangement, with the two cameras mounted one above the other, has allowed the simultaneous imaging of the flow field from the opposite sides of the rudder in the configuration A.

In both the configurations, the laser beam was horizontally aligned and, then, 90° rotated by a 45° mirror to generate a vertical light sheet. A second mirror reflecting the light sheet was placed on the top-window of the facility in order to compensate the lack of light in the regions at the leading and trailing edges of the rudder, where the curvature is such to locally block the laser sheet passage. The alignment of the reflected laser sheet was performed adjusting the orientation of the second mirror to make its trace coinciding with that of the conveyed laser sheet on the 45° mirror. The uncertainty of this operation is estimated to be less than half the thickness of the laser sheet which corresponds to <0.04°. The use of a long focal

length spherical lens allowed minimizing the differences in the thickness of the conveyed and the reflected laser sheets, making them practically negligible in the measuring area.

The PIV acquisition was conditioned upon the passage of the propeller reference blade for a selected angular position. This was carried out synchronizing the PIV acquisition to a TTL OPR (i.e., Once/Revolution) signal, supplied by a signal processor fed by a 3,600 pulse/s rotary incremental encoder, mounted on the propeller dynamometer. Once triggered, the PIV synchronizer supplies a TTL signal to the two cross-correlation cameras and to a double-cavity Nd-Yag laser (200 mJ/pulse at 15 Hz) according to the timing diagram (150 μs time between pulses). The length of each laser pulse was 7 ns.

The mean particle displacement between pulses was about 6 px. Assuming the level of uncertainty of the PIV algorithm to be <0.1 px, the corresponding error can be estimated to be <2% of the average velocity.

The statistical analysis was performed on a population of 500 images/phase, acquired at each propeller phase in the range 0–85°, 5° step. The amplitude the confidence interval Δu , estimated by the t Student distribution over a population of $N = 500$ samples (i.e., $\Delta u = \pm t_{0.975}(N) \times \text{RMS}/(N - 1)^{0.5}$, where $t_{0.975}(N)$ is the t Student value corresponding to the confidence level of $\alpha = 97.5\%$ and the sample size of N), was about 1/11 of the measured root mean square (RMS), and, thus, ranged from 0.01 m/s (e.g., propeller wake inter-spiral region) to 0.1 m/s (e.g., tip and hub vortex region, near wake of the rudder).

Instantaneous velocity fields were acquired from a distance of 500 mm from the facility side window, using a 60 mm lens with 5 f number and imaging an area of about 160×130 mm².

The flow field evolution was reconstructed reassembling six different patches (i.e., 3/camera) by which the whole investigation area was scanned. In this regard, the PIV system was mounted on a two-axis translation stage in order to be moved between adjacent regions with the adequate precision. This operation was executed with an accuracy of 0.1 mm in order to minimize any misalignment during patch reassembling. In addition, patches were overlapped partially in order to compensate any minimal camera misalignment during the final reconstruction of the flow field evolution.

Facility water was seeded with 30–40 μm silver-coated hollow glass spherical particles with high diffraction index and density of about 1.1 g/cm³.

Prior the analysis, images were preprocessed. This was carried out subtracting the mean gray image obtained over the whole image population for a given patch and phase angle. This procedure allowed the complete removal of any unwanted background and reflection, resulting in an improved signal-to-noise ratio of the processing. In the

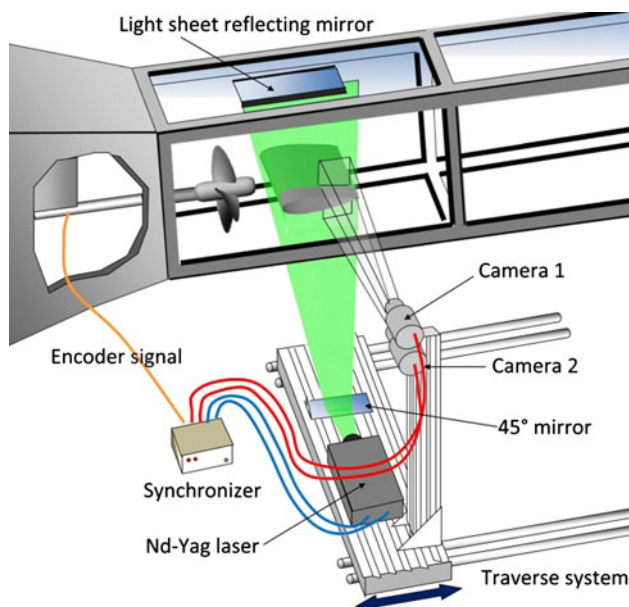


Fig. 2 PIV experimental set-up

present case, the mean image subtraction was experienced to be more efficient than the minimum gray level image subtraction method, even if only particles with gray level higher than the mean contributed to the cross-correlation peak.

Image analysis was performed combining the discrete offset technique (Di Florio et al. 2002) and the iterative image deformation method (Scarano and Riethmuller 2000; Scarano 2002). The displacement field obtained with the first analysis method was used to distort the images (Huang et al. 1993), upon which direct cross-correlation was applied to calculate the “corrected” velocity field. Such a newly updated velocity predictor was used to re-distort the original images subsequently. This process was repeated iteratively until a convergence criterion was verified.

The combined use of the discrete window offset technique and the iterative image deformation method allowed handling successfully the problem to widen the dynamic range of the measurement and to increase the spatial resolution. Both these aspects are relevant in the experimental survey of the flow field around a propeller–rudder configuration in which high velocity gradients and a wide scale range of vortical structures typically occur.

The adopted processing set-up was composed by a 3-step discrete offset method with a final window size of $32 \times 28 \text{ px}^2$ (i.e., interrogation windows stretched slightly in the streamwise direction) and a grid spacing between the vectors of 10 pixels (i.e., 66% overlap). The corresponding separation among adjacent vectors was 1.25 mm. This value was adequate to reconstruct the overall evolution mechanisms of the tip vortex filaments whose characteristic length scale is of the order of 5–10 mm and, thus, such to fulfill the sampling theorem.

The image deformation was then performed through 4 iterations with a local Gaussian weighting filter applied to the predictor field and a Gaussian sub-pixel interpolation fit.

A validation procedure was applied to PIV data to detect and replace spurious vectors. The ratio of the spurious to the total vectors ranged from 0.5 to 2%, depending on the position of the measurement plane (i.e., the density of spurious vectors was larger in the planes intersecting the rudder and the propeller boss).

2.4.2 LDV experimental set-up

A sketch of the LDV experimental set-up is shown in Fig. 3. Flow velocity was measured by means of a two-component LDV system, which consisted of a 6 W Argon Laser, a two-component underwater fiber optic probe (wavelengths of 514.5 and 488 nm) and a 40 MHz Bragg cell for the velocity versus ambiguity removal. The probe

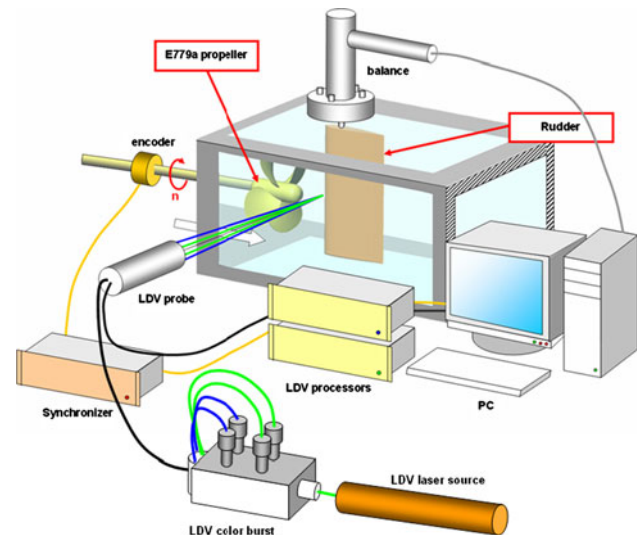


Fig. 3 LDV experimental set-up

was equipped with a spherical lens having the diameter of 61 mm and the focal length of 500 mm. The ellipsoidal probe volume had a length of about 2.7 mm and a diameter of about 0.164 mm.

LDV signal processing was executed by the TSI FSA 3500 processor.

In the adopted LDV system, the probe worked in backscatter and allowed measuring two orthogonal components of velocity field simultaneously. During the experiments, the probe was arranged to measure the axial and vertical components of the velocity in a fixed frame.

The 3-D velocity survey was performed in two separate steps rotating the experiment of 90° , similarly to the experiment of Felli et al. (2009a). More specifically, two configurations with the rudder fixed on the top and side window of the test section were used to resolve the U – W and the U – V velocity components, respectively.

A special target with known position with respect to the center of the propeller disk was used to minimize any uncertainty in the overlapping of the grids used in the two configurations.

The underwater probe was set up on a computer-controlled traverse which allowed getting a displacement accuracy of 0.1 mm in all the directions and to achieve a high automation of the LDV system.

Particular care was required during the initial location of the measurement volume to reduce positioning errors of the two optical configurations. This was carried out by aligning the measurement volume on a special target with known position as to the propeller disk center.

The tunnel water was seeded with $1 \mu\text{m}$ titanium dioxide (TiO_2) particles in order to improve the Doppler signal processor data rate. Water seeding was performed at the start of the tests, because it was experienced that the seed

particle density remains almost constant for a long time in the facility.

Data acquisition was accomplished by using a personal computer, while the post-processing analysis, requiring several GBytes of data storage and large computational resources, was performed on a workstation.

Phase sampling of the velocity signal was carried out by a rotary 7,200 pulse/revolution encoder and a synchronizer; the latter provides the digital signal of the propeller position to the TSI RMR (Rotating Machine Resolver).

The correspondence between the randomly acquired velocity bursts and the propeller angular position was carried out by phase sampling techniques. The adopted procedure was the tracking triggering technique [TTT] (Stella et al. 2000) which was proved to allow the acquisition process to be efficient and fast (Stella et al. 2000; Felli and Di Felice 2005). In this approach, velocity samples are arranged within angular slots of constant width, depending on the angular position of the reference blade at the measurement time. The statistical analysis is then performed for each slot to obtain phase-locked mean velocity and turbulence intensity information.

In the present study, the phase-locked statistics concerned 360 overlapped slots with 2° width.

Velocity samples were recorded during 60 s at a data rate which varied in the range of approximately 0.4–3 kHz. This resulted in an on-average statistical population which ranged from approximately 130 to 1,000 samples per slot and, hence, in a statistical uncertainty which is estimated to vary from 0.18 to 2.5% of the free-stream velocity.

Transit-time averaging technique was used for the calculation of the moments in order to eliminate the velocity bias.

3 Test matrix and experimental conditions

Tests were executed at the free-stream velocity of $U_\infty = 5$ m/s and the propeller revolution speed of $n = 25$ rps, corresponding to the advance ratio, J , of 0.88. Based on the rudder chord and the free-stream velocity, the nominal Reynolds number was around $Re = 1.36 \times 10^6$. It should be added that velocities induced by the propeller led to an effective Reynolds of 1.63×10^6 at the leading edge of the rudder. Rudder was fixed at zero deflection angle and with the leading edge at about $x = R$ from the propeller disk. In these conditions, the error due to the blockage effect was estimated to be within the uncertainty of the measurement.

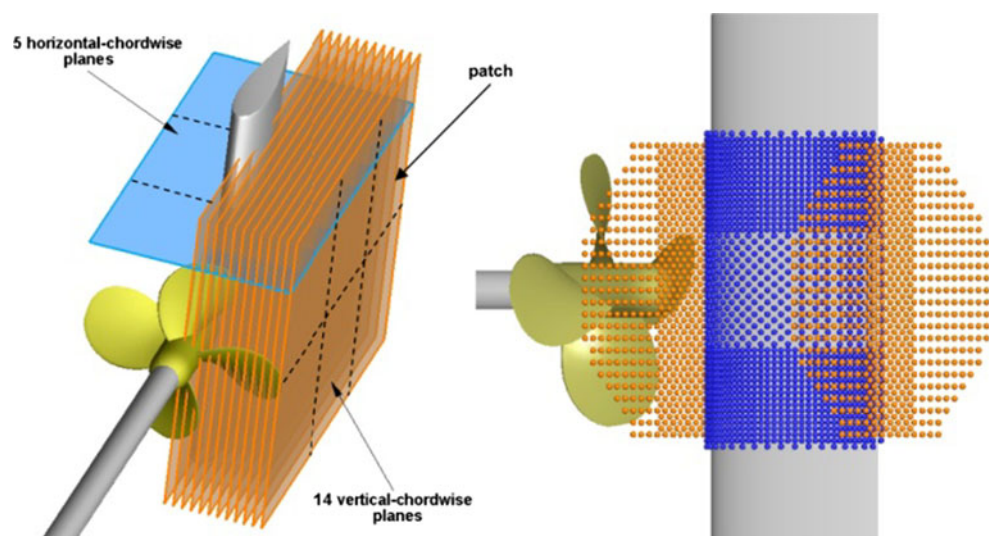
The test matrix includes:

- PIV measurements along 5 horizontal chordwise and 14 vertical chordwise sections of the wake, with a 5 mm separation.
- LDV measurements along 2 transversal sections of the wake just in front and behind the rudder, each having a grid of about 700 points, and all along the rudder surface, where a grid with 1,200 points thickened in the tip vortex region was used.
- Time-resolved visualizations at different values of cavitation number σ_N (i.e., $\sigma_N = \frac{P - P_V}{0.5 \cdot \rho \cdot (n \cdot D)^2}$ with P and P_V the reference pressure measured at the propeller axis and the vapor pressure, respectively, ρ the water density, n the propeller speed and D the propeller diameter).

For the sake of conciseness, only part of the data set is reported in this paper.

A sketch of the PIV planes and the LDV measurement grid is reported in Fig. 4.

Fig. 4 PIV planes (*left*) and LDV measurement grids (*right*)



4 Experimental results

The flow field evolution at the zero rudder deflection is described hereinafter through the representation of the phase-locked velocity field during the revolution period, according to the following equation:

$$\langle V(x, y, z) \rangle = \sum_{i=1}^N V[x, y, z, \theta_0 + 2\pi \cdot (i - 1)], \quad N = 500,$$

$$\theta_0 \in [0^\circ, 5^\circ, 10^\circ, \dots, 85^\circ]$$

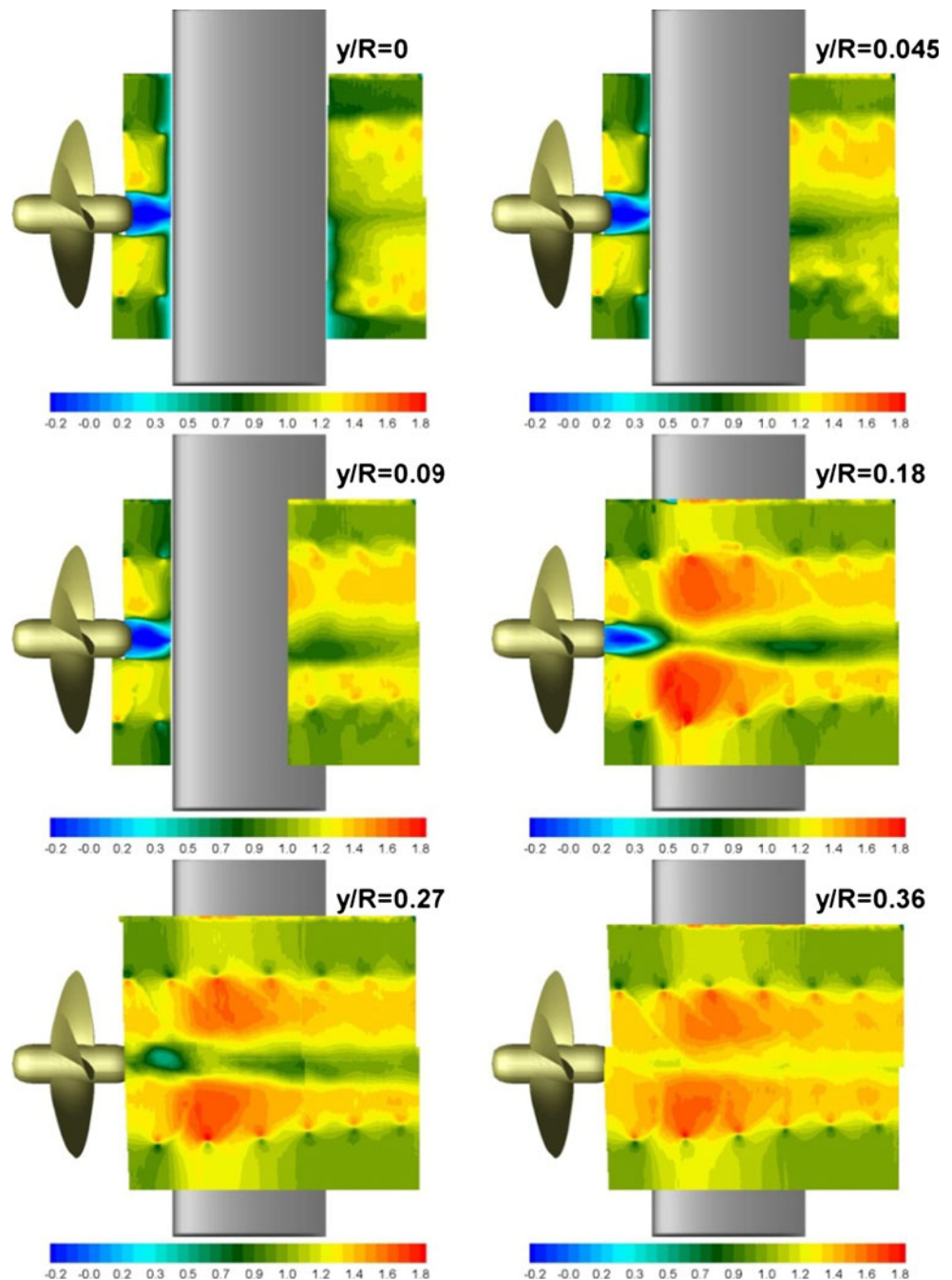
with θ_0 representing the angular position of the propeller reference blade and $\langle \dots \rangle$ the average over the N samples acquired at the same phase, also named phase average.

For the sake of conciseness, only the most representative results are reported.

4.1 Flow field evolution

An overview of the phase-locked distribution of the axial velocity and the Y vorticity as measured along six vertical

Fig. 5 Phase-locked PIV measurements along six longitudinal–vertical planes of the wake: axial velocity. Propeller at $\theta = 15^\circ$



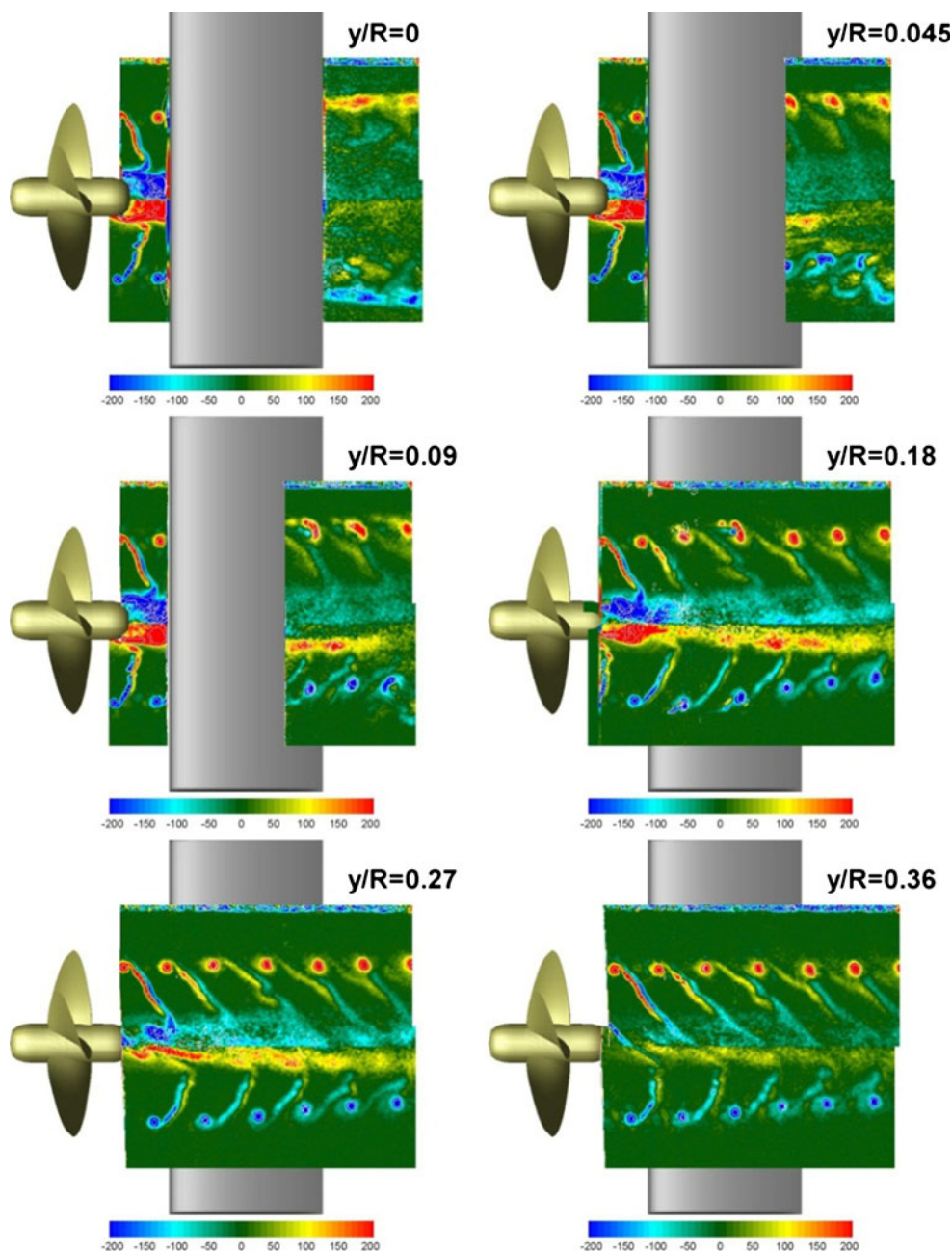
chordwise planes ranging from $y/R = 0$ to $0.36R$ is documented in Figs. 5 and 6. Figures 7 and 8 represent the same quantities along the horizontal chordwise plane at $z = 0.95R$ (Fig. 7) and the transversal planes just upstream and downstream of the rudder (Fig. 8). Figure 9 shows the distribution of the axial velocity and the Y vorticity along the rudder surface.

The distribution of the velocity around the rudder is skew-symmetric respecting to the rudder mid-plane; this is the consequence of either the on-average-axis-symmetric distribution of the velocity field in the propeller wake, when the propulsory operates in open water, and the

position of the rudder, whose symmetry plane is aligned to the propeller axis.

In the present case (i.e., propeller rotating in the clockwise direction, as seen from aft), flow acceleration is larger in the starboard side of the propeller wake (i.e., on the upper part of the rudder relative to the propeller shaft or x axis as seen in Fig. 5) compared to the port side of the wake (i.e., on the lower part of the rudder in Fig. 5). This is documented in the contour plots of Figs. 5 and 7, respectively, which shows a more intense distribution of axial velocity right in the starboard upper and portside-lower regions.

Fig. 6 Phase-locked PIV measurements along six longitudinal-vertical planes of the wake: out of plane component of the vorticity. Propeller at $\theta = 15^\circ$



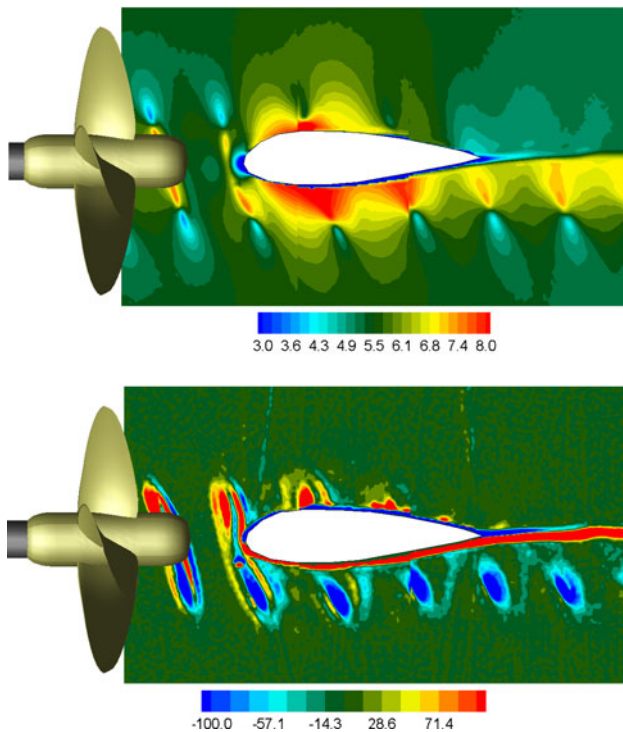
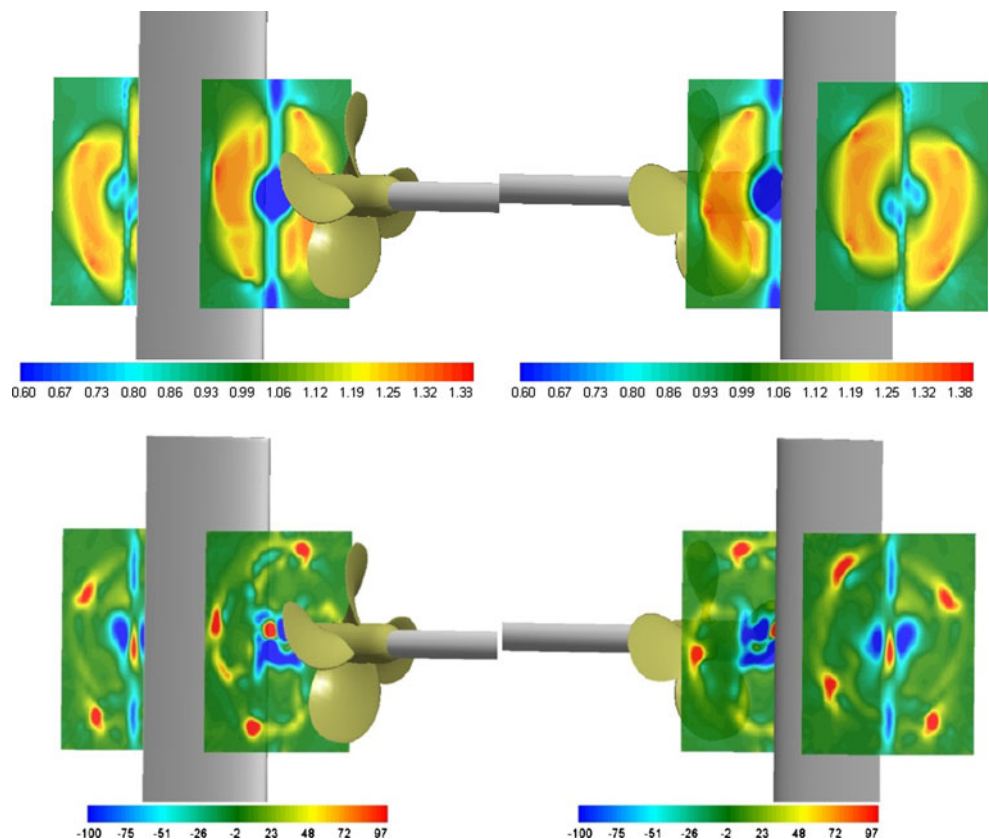


Fig. 7 Phase-locked PIV measurements along the longitudinal–horizontal plane at $z = 0.95R$: axial velocity (*top*) and out of plane component of the vorticity (*bottom*). Propeller at $\theta = 0^\circ$

Fig. 8 Phase-locked LDV measurements along the transversal planes just in front and behind the rudder: axial velocity (*top*) and out of plane component of the vorticity (*bottom*). Propeller at $\theta = 0^\circ$



The corresponding spanwise distribution of the side force, i.e., $F_z(y)$, is, thus, supposed to keep skew-symmetric on average and the corresponding resultant theoretically zero. A non-zero resultant of the side force was found in Felli et al. (2009a, b) instead: however, here the rudder was at an offset respecting to the propeller axis and with a finite-length geometry.

An estimation of the on-average distribution of the side force $F_z(y)$ was undertaken considering the spanwise distribution of the circumferential average of the hydrodynamic incidence (i.e., $\beta = \text{atan}\left(\frac{W(s)}{U(s)}\right)$) and the velocity projection over the x – z plane U_{eff} (i.e., $U_{\text{eff}} = \sqrt{U(s)^2 + W(s)^2}$), analogously to Felli et al. (2009a). The result is documented in Fig. 10 where $F_z(y)$ is here normalized with $\rho \cdot n^2 \cdot D^4$. The side force shows clearly a skew-symmetric distribution which presents its maximum at about $s/R = 0.3$, where s represents the rudder spanwise abscissa with the origin at the intersection with the propeller axis, then, decays to 0 at about $s = 1.13R$ describing a nearly linear law.

In front of the rudder, the propeller slipstream slows down more and more as it approaches the stagnation point. The rate of the slowdown was estimated considering the distribution of the circumferential-averaged derivative of

Fig. 9 Phase-locked LDV measurements along the rudder surface: axial velocity component (*left*) and horizontal component of the vorticity (*right*). Propeller at $\theta = 0^\circ$

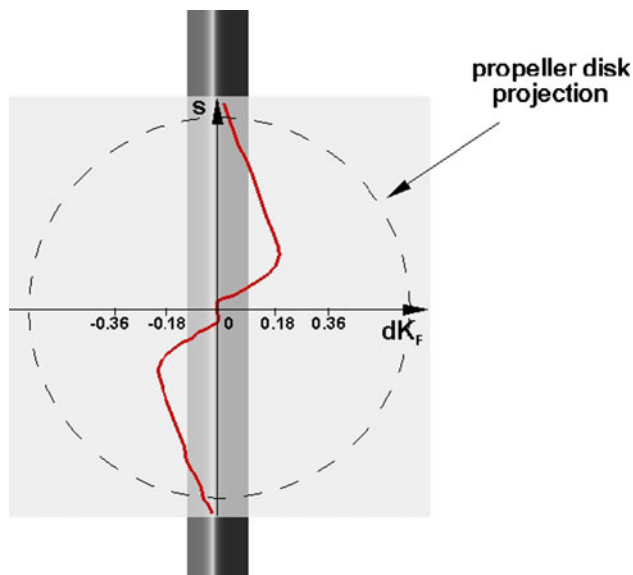
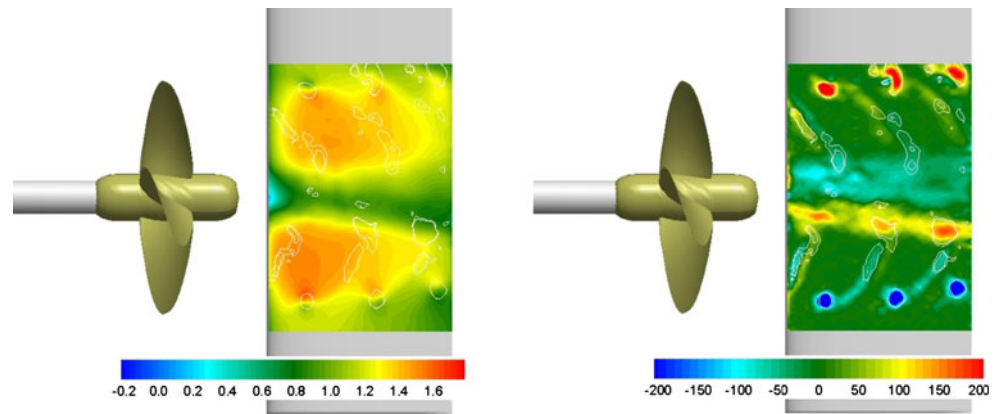


Fig. 10 Circumferential-averaged distribution of the side force coefficient $dK_F(s)$

the axial velocity along the streamwise direction (i.e., $\partial U/\partial x$), calculated over the section passing through the symmetry plane of the rudder (i.e., $z = 0$). At the test condition (i.e., $U_\infty = 5$ m/s, $J = 0.88$), the slipstream deceleration, nearly zero down to about $0.17R$ from the leading edge of the rudder, tends to increase more and more streamwise and to reach the maximum in the stagnation point. This is documented in Fig. 11 in which the distribution of the streamwise derivative of the axial velocity is shown in a contour plot (top) and in a 2-D graph (below figure) which represents the same quantity along a longitudinal line at $z/R = -0.6$.

The distribution of the vorticity fluctuations measured by PIV is documented in Fig. 12. Figure 13 shows the distribution of the turbulent kinetic energy as measured by LDV along the transversal plane just behind the rudder. More specifically, the following considerations are worth to be outlined from the analysis of Figs. 12 and 13:

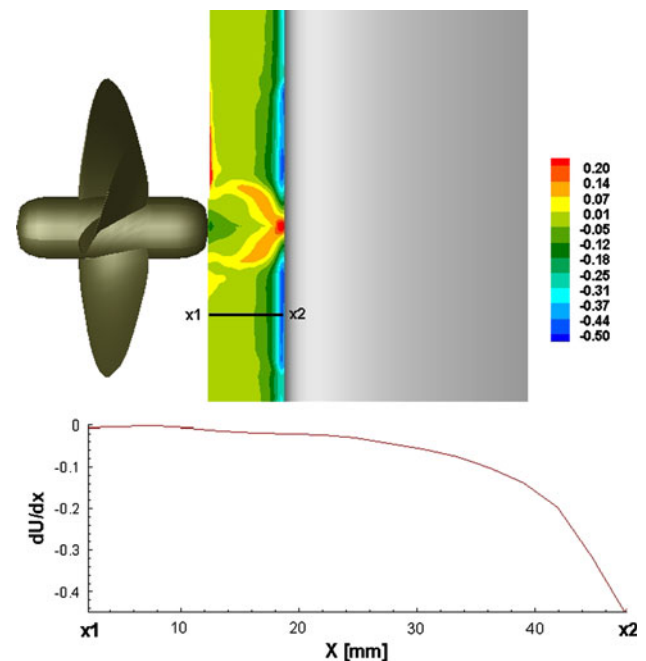
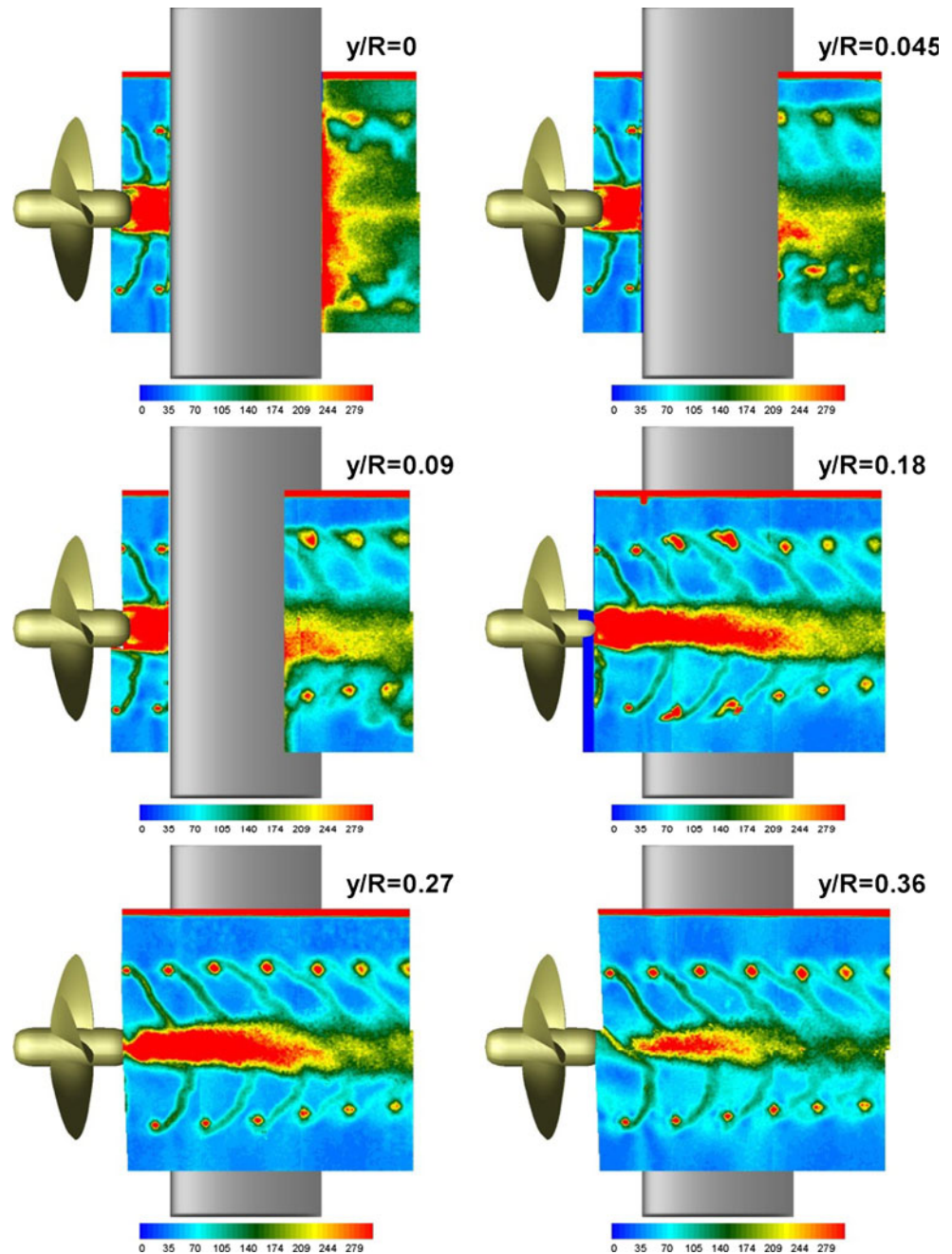


Fig. 11 Propeller slipstream slow down in front of the rudder: circumferential-averaged distribution of $\partial U/\partial x$ (top). Extraction of the $\partial U/\partial x$ distribution along the line from x_1 to x_2 (bottom)

1. Vorticity fluctuations are maximum corresponding to the traces of the propeller structures (i.e., tip and hub vortices, blade wake trailing vorticity) and all along the trailing wake of the rudder.
2. The intensity of the vorticity fluctuations in the wake of the rudder is very strong just behind the trailing edge of the appendage and, then, reduces rapidly streamwise (see iso-contours at $y/R = 0$ in Fig. 12). In addition, the streamwise decay of the vorticity fluctuations occurs with a smaller and smaller extent of the turbulent trace of the trailing wake vorticity either along the streamwise and the transversal directions: this suggests that viscous dissipation has a prevalence over turbulent diffusion effect in the boundary layer eddies of the rudder.

Fig. 12 Phase-locked PIV measurements along six longitudinal-vertical planes of the wake: standard deviation of the out of plane component of the vorticity. Propeller at $\theta = 15^\circ$



3. The marked turbulent nature of the tip vortex rejoining mechanism (Felli et al. 2009a) is clearly documented in contour plots at $y/R = 0.045$ and 0.09 of Fig. 12. The traces of the rejoining face and back filaments of the tip vortex are clearly recognizable in the rotation lower side of Fig. 12 at $y/R = 0.045$ and 0.09 whereas no evidence of the rejoining process is noticed on the rotation upper side. This different behavior is given considering that the rejoining process occurs out of the symmetry plane of the rudder and, precisely, it is shifted toward the direction along which the tip vortex moves (i.e., starboard-wise in the propeller rotation upper plane, portside-wise in the propeller rotation lower plane).
4. Levels of turbulence in the hub vortex are not homogeneously distributed transversally and show maximum values on the starboard side region, as shown in Fig. 13.

4.2 Tip vortex filament evolution

The deceleration of the propeller slipstream in front of the rudder (see Sect. 4.1) causes the tip vortex and the blade

Fig. 13 Phase-locked LDV measurements along the transversal planes just behind the rudder: turbulent kinetic energy at $\theta = 0, 30$ and 60°

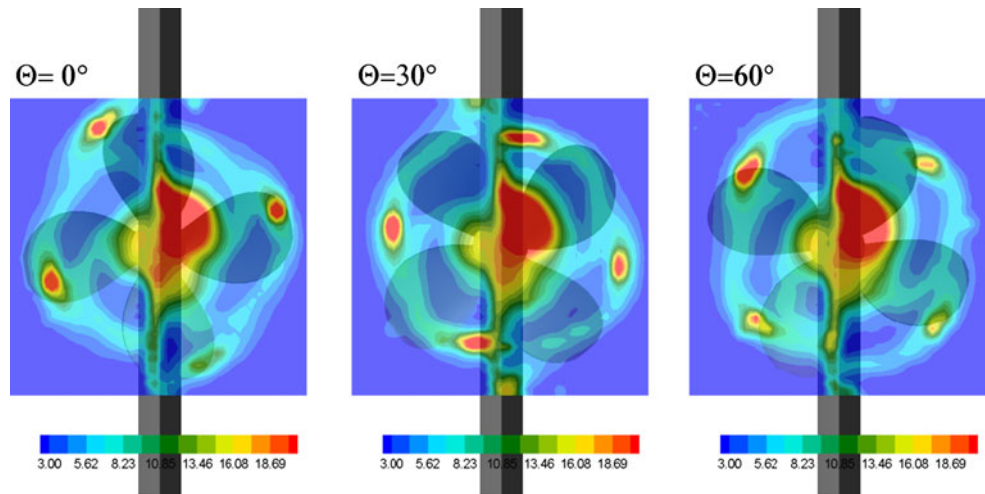
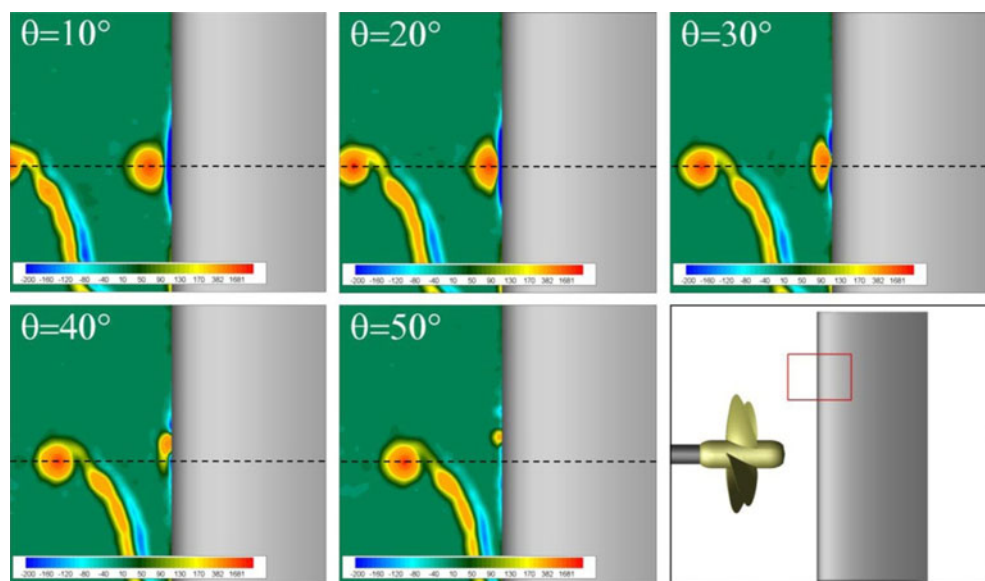


Fig. 14 Dynamics of the tip vortex when approaching the leading edge of the rudder: contour plots of the phase-locked vorticity field in the leading edge region of the rudder. The dashed line is a reference horizontal line to highlight the spanwise outwards displacement of the tip vortex induced by the rudder



trailing wake to deform progressively while approaching the leading edge of the appendage. The evidence of such a deformation is documented in the contour plot of the Z vorticity in Fig. 7.

The presence of the rudder causes the tip vortices to deflect outwards along the spanwise direction, according to the observations by Felli et al. (2009a). In this regard, the occurrence of a vorticity sheet with opposite sign to the incoming tip vortex, in the leading edge of the rudder, proves the validity of the image vortex model for the explanation of the tip vortex deflection along the rudder span (Fig. 14).

During the tip vortex interaction with the rudder surface, cross-diffusion between vorticity in the boundary layer of the appendage and that within the vortex causes vortex lines originating in the tip vortex to reconnect to those within the rudder boundary layer. It results that the tip vortex is incompletely cut by the rudder: vortex lines wrap

about the leading and trailing edges and keep linked the tip vortex parts flowing on the opposite sides of the appendage. The evidence of such a complex structure is given in Fig. 15: the vortex lines wrapping around the leading and trailing edges appear organized in two branches that develop close to the rudder surface on both the sides of the appendage. The signature of the cavitating traces of the branches reduces gradually streamwise as the consequence of the diffusion effects.

This makes not immediate the identification of the two branches by single snapshots when the tip vortex moves toward the trailing edge of the rudder. High-speed visualizations allow a much better understanding of the above evolution mechanism instead.

According to the results of Liu and Marshall (2004), our interpretation of the evolution mechanism of the tip vortex when it interacts with the rudder is documented in Fig. 16. The branch wrapping around the leading edge of the rudder

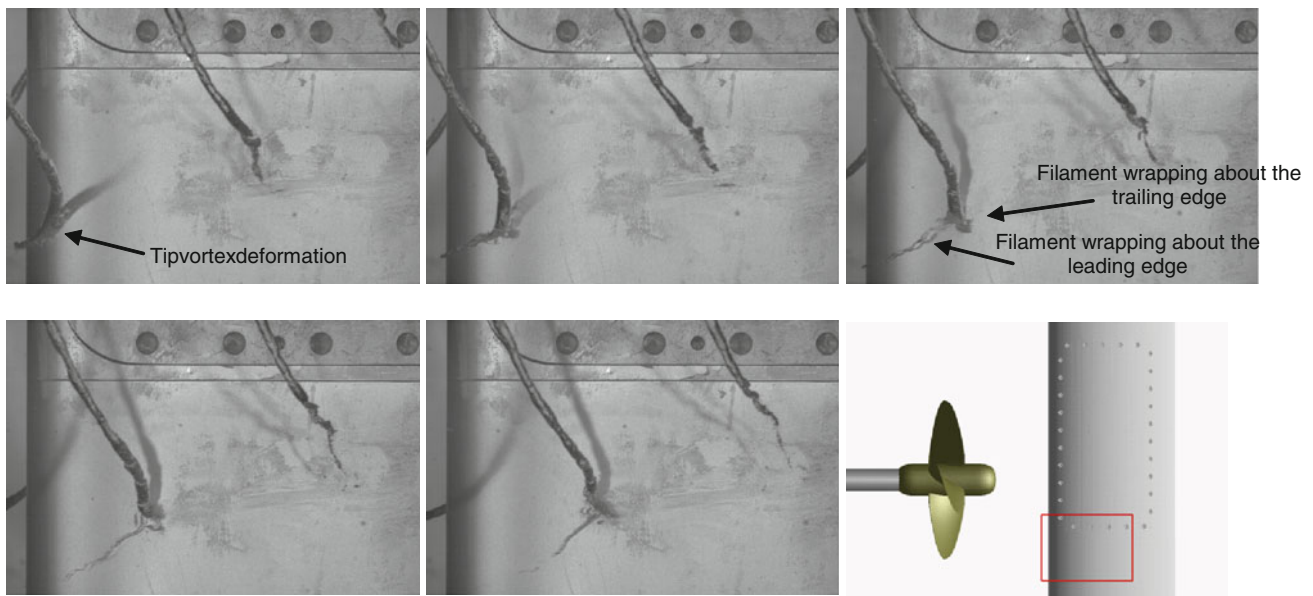


Fig. 15 Tip vortex destabilization while penetrating the rudder: note the cavitating branches that develop close to the rudder surface. Snapshots are spaced 0.0075 s. Visualizations were performed at the cavitation number $\sigma_N = 1.54$ with the rudder at 0 deflection

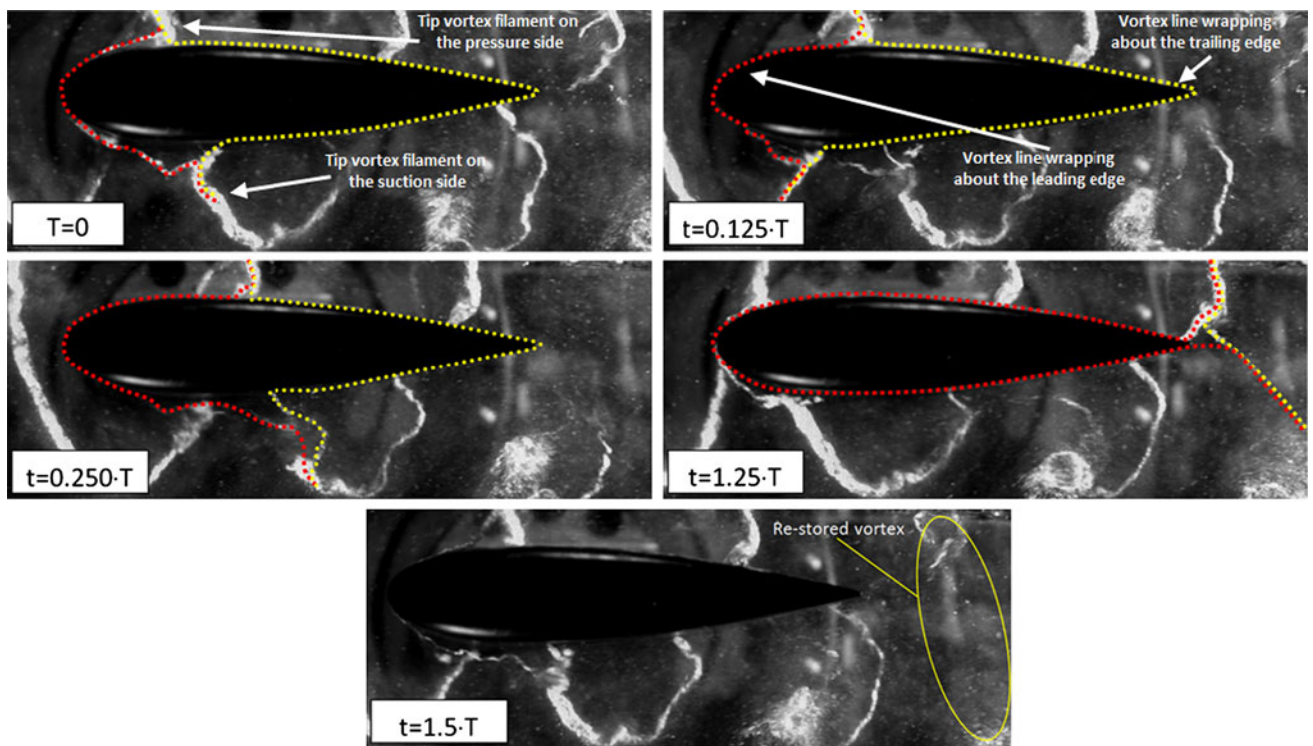


Fig. 16 Reconstruction of the evolution mechanism of the tip vortex when it interacts with the rudder. The traces of the vortex lines wrapping around the leading and trailing edges of the rudder are

highlighted by *red* and *yellow lines*, respectively. Visualizations were performed at the cavitation number $\sigma_N = 1.2$ with the rudder at 0 deflection

(red line in Fig. 16) stretches more and more as the tip vortex filaments are advanced downstream and breaks after the tip vortex has left the trailing edge. The signature of such a progressive stretching is clearly documented in the

planes at $y/R = 0.09$ and 0.18 of Fig. 6 and in the rotation lower region of the vorticity field (right of Fig. 9): the trace of the joining vortex appears as a tail coming out from the back side the tip vortex.

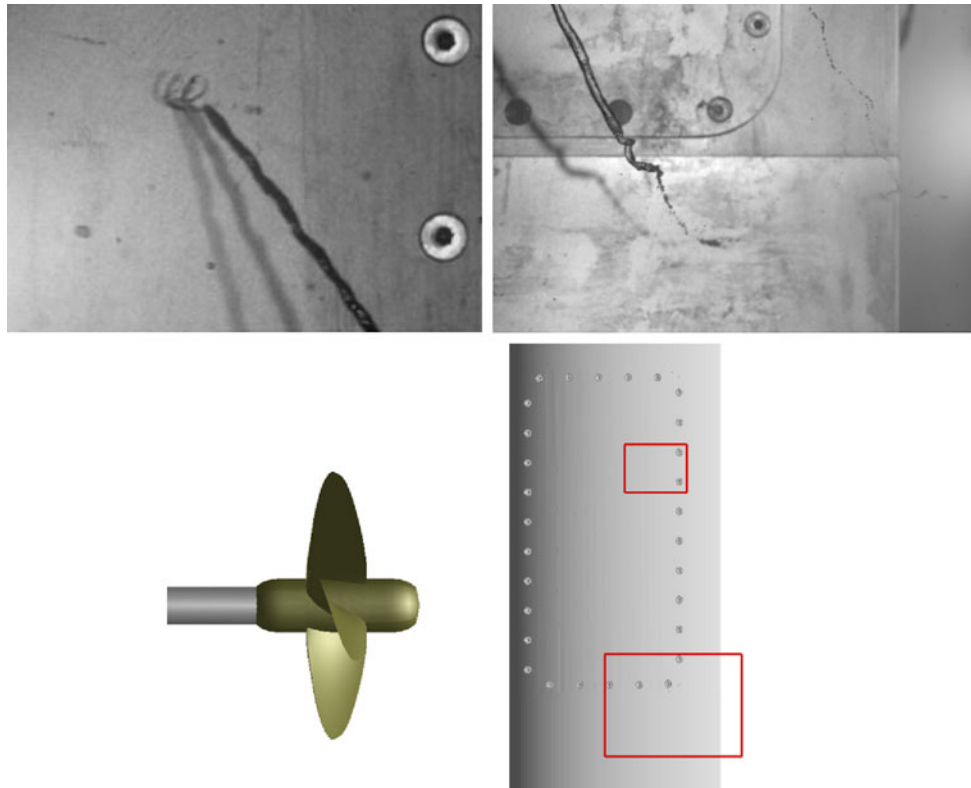


Fig. 17 Spiral breakdown of the tip vortex filaments on the pressure (*top-left*) and suction (*top-right*) sides of the rudder. Visualizations were performed at the cavitation number $\sigma_N = 1.54$ with the rudder at 0 deflection

The progressive stretching of the tip vortex branch wrapping around the leading edge of the rudder is strongly conditioned by the dragging action of the tip vortex filaments and, thus, by the different rate of spanwise displacement that characterizes the tip vortex on the suction and pressure side of the rudder (Fig. 6, plane at $y/R = 0.18$) and about which we refer to Sect. 4.3. On the suction side, the larger and larger inward displacement of the tip vortex filaments tends to drag inward and to stretch the joining filament. A different behavior is instead observed on the pressure side where the joining filament moves nearly streamwise.

From about mid-chord of the rudder, the tip vortex branches wrapping around the trailing edge start to describe a spiral geometry whose radius becomes bigger and bigger streamwise (Fig. 17). The spiral appears rolling up in the opposite direction to the filament rotation and, specifically: clockwise (counter clockwise) for the filament on the pressure (suction) side of the rudder.

The signature of the aforesaid roll up is also captured in the contour plots of the Y vorticity, as documented in the planes at $y/R = 0.09$ and 0.18 of Fig. 6. Here, the spiraling geometry of the vortex filament is resolved as a vorticity core (clockwise rotating in the pressure side) surrounded by a counter-rotating vorticity sheet which suddenly appears

at about the mid-chord region of the rudder. This behavior seems to be correlated to the filament wrapping observed on the top left-hand side of Fig. 17: the vorticity core might be induced by the overall roll up of the spiral and the surrounding vorticity sheet might be ascribable to the vorticity of the vortex filament. A higher resolution measurement focused on this region might provide better information to draw conclusions about this point.

The geometrical characteristics of the spiral appear different in the pressure and suction side filaments, as easily verifiable comparing the snapshots of Fig. 17. In particular, the difference concerns mainly the pitch and the aperture of the spiral, which are respectively smaller and larger in the filaments moving along the pressure side of the rudder.

PIV gives an interesting perspective of the tip vortex rejoining mechanism behind the trailing edge of the rudder. Specifically, the distribution of the Y vorticity in the plane at $y = 0.05c$ (Fig. 18) shows the signature of the vortex line wrapping about the trailing edge that appears suddenly to keep linked the filaments coming from the face and the back surfaces of the rudder downstream of the rudder.

Correspondently, the iso-contours of the Reynolds stresses highlight the occurrence of a complex shear region

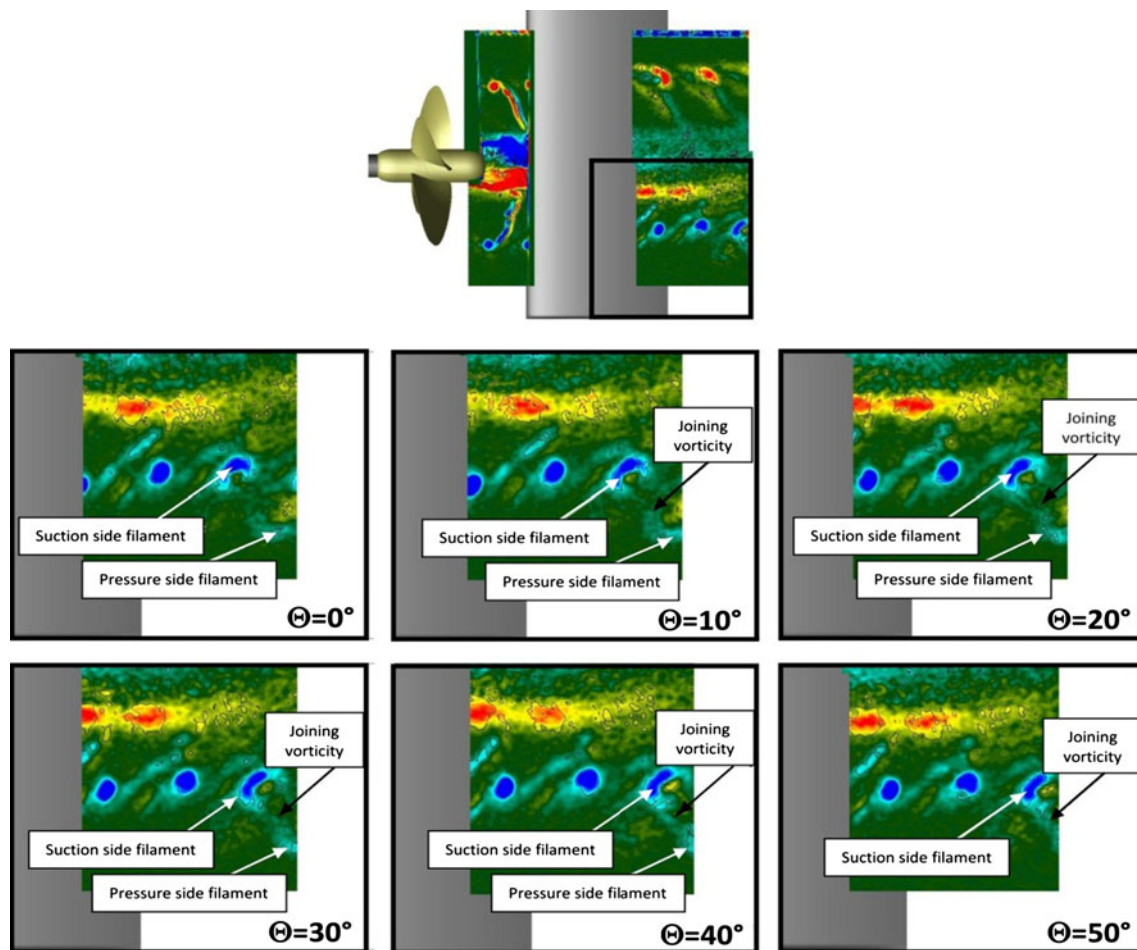


Fig. 18 Tip vortex rejoining mechanism: phase-locked evolution of the vorticity field along the longitudinal–vertical plane at $y/R = 0.09$

which extends between the traces of the face and the back filaments (Fig. 19).

4.3 Spanwise misalignment of the tip vortex filament

The interaction with the rudder causes a spanwise displacement of the tip vortex filaments on the opposite faces of the appendage which tends to increase more and more chordwise. The analysis of the tip vortex traces outlines that the rate of such a spanwise displacement is particularly marked for the filaments moving along the suction sides of the rudder. Instead, on the pressure side, the traces of the tip vortices describe a nearly horizontal trajectory. The features of such a spanwise misalignment are described in the vorticity fields of Fig. 6 and right of Figs. 7 and 9, the latter documenting the vorticity field measured along a plane at about 1 mm from the rudder surface.

We argue that two are the reasons of this misalignment:

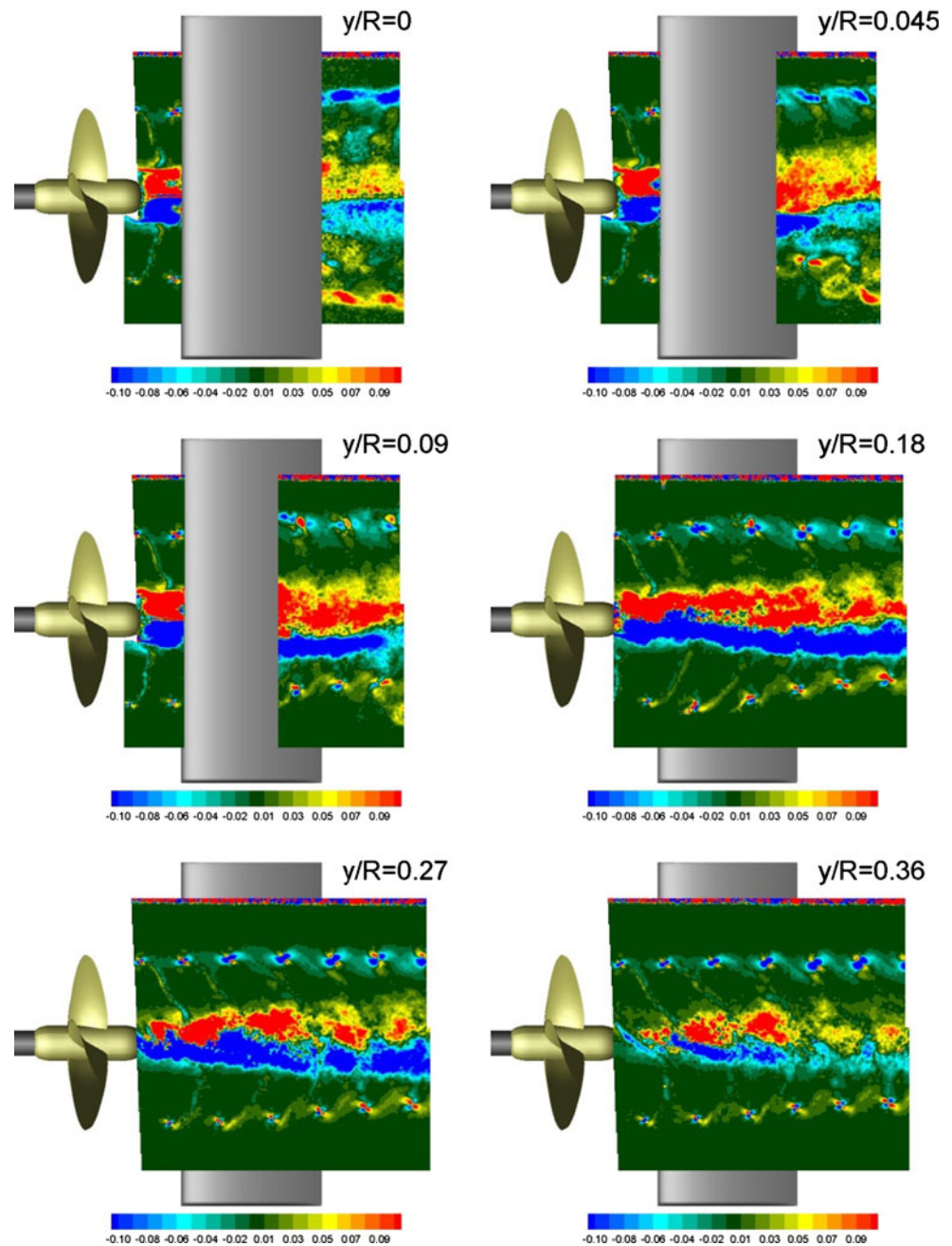
- (1) In both the rotation upper and lower regions, the larger dynamic pressure in the propeller wake makes increasing the intensity of the pressure field along the

spanwise direction moving outwards from the radial position where propeller develops maximum thrust (i.e., $r = 0.7R$) (see picture at top-right of Fig. 20 which shows the distribution of the total pressure on the rudder surface). Therefore, the corresponding spanwise gradient of the pressure field is inward-oriented locally, as represented by the yellow arrow in Fig. 20.

- (2) The effect of the image vortex is such to displace the tip vortices upward (downward) in the port side (starboard side) of the rudder when the propeller is rotating clockwise, as explained in Felli et al. (2006a).

According to what observed in (1) and (2), the convective motion induced by the image vortex occurs with a favorable (adverse) pressure gradient in the suction (pressure) side of the rudder, and, thus, results in a larger displacement. In the pressure side of the rudder the opposite is true, i.e., smaller displacement is observed. It follows that such a different trend results in more and more larger spanwise deviation between corresponding tip vortex filaments which attains its maximum at the trailing edge of the

Fig. 19 Phase-locked PIV measurements along six longitudinal–vertical planes of the wake: in-plane component of the Reynolds stresses. Propeller at $\theta = 0^\circ$



rudder. The contour plots of Fig. 13 show this spanwise misalignment from a different perspective.

5 Conclusions and future works

The present paper deals with the propeller–rudder interaction mechanisms and it is focused on the analysis of the evolution of the propeller vortical structures under the interference of the rudder.

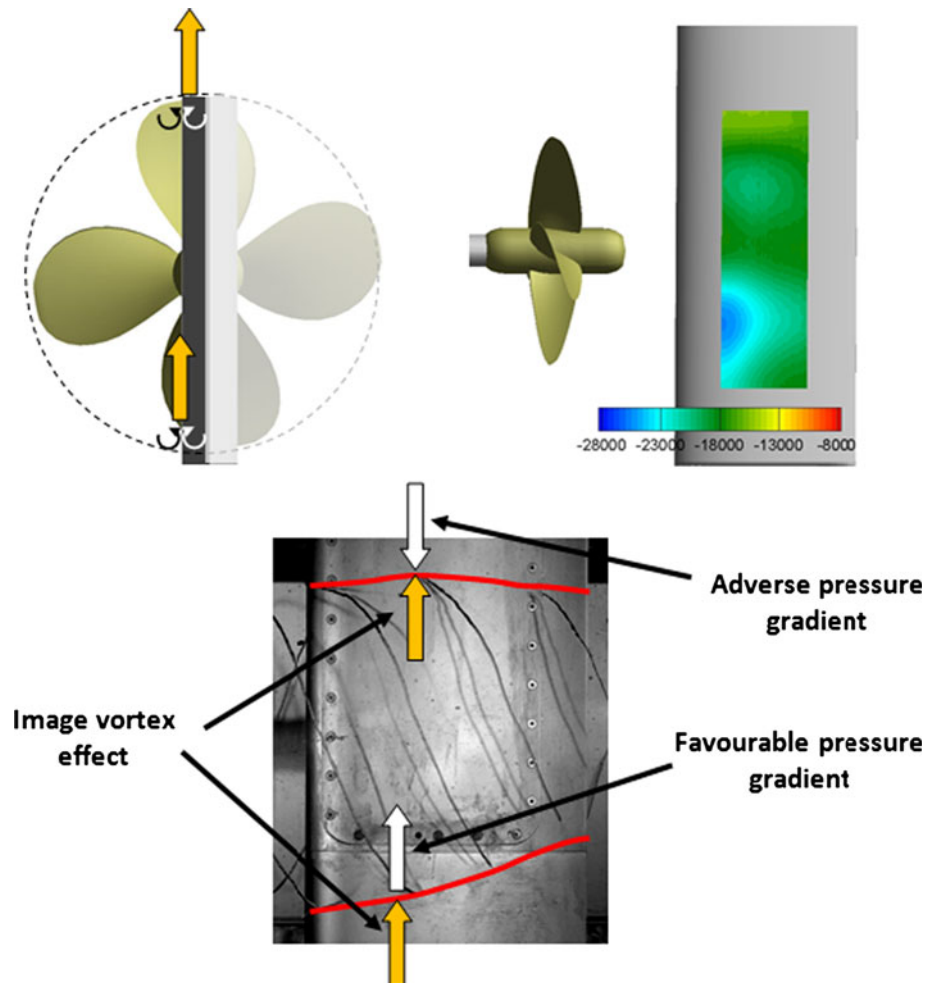
The study concerned a wide experimental activity in which velocity measurements by phase-locked PIV and

LDV and time-resolved visualizations were used to investigate the flow field around a propeller–rudder configuration operating in open water.

Collected data allowed describing the major flow features that distinguish the interaction of the propeller tip and hub vortices with the rudder, with special emphasis to the unsteady flow aspects. Specifically, the following phenomena were deeply investigated and are worth to be outlined:

- The impact mechanism of the propeller tip vortices against the rudder undergoes with a marked bending

Fig. 20 Explanation of the different spanwise displacement of the pressure and suction-side filaments: effect of the image vortex (*top-left*), pressure distribution along the rudder surface (*top-right*) (courtesy of Felli et al. 2010), effect of the image vortex and the pressure gradient on the trajectories of the pressure and suction-side filaments



that increases more and more while the vortex is approaching toward the leading edge of the appendage. The interaction with the rudder moves the tip vortex filaments outward according to the image vortex model.

- The tip vortex penetration into the rudder and the following rejoining process behind the trailing edge are characterized by a complex dynamics. The vortex lines originating in the tip vortex organize in two-branch structures that develop close to the rudder surface, on both the sides of the rudder. These branches are supposed to wrap around the leading and trailing edges of the rudder and keep linked the tip vortex parts flowing on the opposite sides of the appendage through the vorticity of the boundary layer. The evidence of such a mechanism is provided by the results of the time-resolved visualizations in cavitating regime flow mainly.
- The mechanism governing the different spanwise displacement of the tip vortex filaments running on the pressure and suction sides of the rudder is strongly depended on the local distribution of the pressure gradient along the span and the rotation direction of the

tip vortex. It results that the filaments flowing along the suction sides of the rudder undergo a larger inwards displacement, the displacement induced by the image vortex occurring with a favorable pressure gradient locally.

The analysis of the instantaneous velocity signals is considered a suitable tool to further investigate into the complex dynamics of the tip vortex filaments during the interaction with the rudder. In this regard, a more in-depth and accurate analysis of the destabilizing mechanisms of the propeller vortices during the interaction with the rudder is going to be performed focusing in the tip vortex region. Moreover, the marked unsteady and three-dimensional nature of the flow field suggests to integrate the analysis with stereo-PIV and time-resolved PIV measurements. The application of techniques by which conditioning the PIV acquisition with signals for accelerometers or pressure sensors might be worth of consideration to investigate onto the correlation between the dynamics of the propeller wake and the induced perturbation on the rudder in terms of noise, vibrations and fatigue stresses.

The effect of the propeller inflow on the interaction between the tip vortex and the rudder represents an issue to be dealt with because closer to a real operative condition in the naval propulsion field.

Acknowledgments This work was supported by the Italian Ministry of Defence in the framework of the research project “PRIAMO”. The authors are also grateful Mr. D. Reali that supported the experimental activity in the framework of his Master Degree thesis.

References

- Anschau P, Mach KP (2009) Stereoscopic PIV measurements of rudder flow and vortex systems in the towing task. *ATM* 09, Nantes
- Di Felice F, Di Florio D, Felli M, Romano GP (2004) Experimental investigation of the propeller wake at different loading conditions by particle image velocimetry. *J Ship Res* 48:168–190
- Di Florio G, Di Felice F, Romano GP (2002) Windowing, re-shaping and reorientation interrogation windows in particle image velocimetry for the investigation of shear flows. *Meas Sci Technol* 13:953–962
- Felli M, Di Felice F (2004) Analysis of the propeller-hull interaction by LDV phase sampling techniques. *J Vis* 7(1):77–84
- Felli M, Di Felice F (2005) Propeller wake analysis in non-uniform inflow by LDV phase sampling techniques. *J Marine Sci Technol* 10(4):159–172
- Felli M, Di Felice F, Guj G, Camussi R (2006a) Analysis of the propeller wake evolution by pressure and velocity phase measurements. *Exp Fluids* 41:441–451
- Felli M, Greco L, Colombo C, Salvatore F, Di Felice F, Soave M (2006b) Experimental and theoretical investigation of propeller-rudder interaction phenomena. In: *Proceedings of the 26th symposium on naval hydrodynamics*, Rome
- Felli M, Camussi R, Guj G (2009a) Experimental analysis of the flow field around a propeller-rudder configuration. *Exp Fluids* 46:147–164
- Felli M, Falchi M, Di Felice F (2009b) PIV analysis on the mechanism of evolution and interaction of the propeller tip vortices with a rudder. In: *Proceedings of the 8th international symposium on particle image velocimetry: Piv09*, Melbourne
- Felli M, Falchi M, Pereira F, Di Felice F (2010) Dynamics of the propeller wake structures interacting with a rudder. In: *Proceedings of the 28th symposium on naval hydrodynamics*, Pasadena, California
- Huang HT, Fielder HF, Wang JJ (1993) Limitation and improvement of PIV; part II: particle image distortion, a novel technique. *Exp. Fluids* 15:263–273
- Kracht AM (1992) Ship propeller rudder interaction. In: *Proceedings of the 2nd international symposium on propeller and cavitation*. Hangzhou, China
- Liu X, Marshall JS (2004) Blade penetration into a vortex core with and without axial core flow. *J Fluid Mech* 519:81–103
- Lücke T, Streckwall H (2009) Cavitation research on a very large semi spade rudder. In: *Proceedings of the first international symposium on marine propulsors, SMP'09*, Trondheim
- Molland AF, Turnock SR (1992) Wind tunnel investigation of the influence of propeller loading on ship rudder performance. The Royal Institution of Naval Architects, London
- Paik BG, Kim KY, Ahn JW, Kim YS, Kim SP, Park JJ (2008) Experimental study on the gap entrance profile affecting rudder gap cavitation. *Ocean Eng* 35:139–149
- Scarano F (2002) Iterative image deformation methods in PIV. *Meas Sci Technol* 13:1–19
- Scarano F, Riethmuller ML (2000) Advances in iterative multigrid PIV image processing. *Exp Fluids* 29:51–60
- Shen YT, Jiang CW, Remmers KD (1997a) Twisted rudder for reduced cavitation. *J Ship Res*, pp 41–44
- Shen YT, Remmers KD, Jiang CW (1997b) Effect of ship hull and propeller on rudder cavitation. *J Ship Res*, pp 41–43
- Stella A, Guj G, Di Felice F, Elefante M (2000) Experimental investigation of propeller wake evolution by means of LDV and flow visualizations. *J Ship Res* 44(3):155–169